



Contents lists available at ScienceDirect

Extreme Mechanics Letters

journal homepage: www.elsevier.com/locate/eml

Triboelectric rotational speed sensor integrated into a bearing: A solid step to industrial application

Zhijie Xie^{a,*}, Jiewei Dong^a, Yikang Li^b, Le Gu^a, Baoyu Song^a, Tinghai Cheng^{b,c,*},
Zhong Lin Wang^{c,d,**}

^a School of Mechatronics Engineering, Harbin Institute of Technology, Harbin, Heilongjiang, 150001, China

^b School of Mechatronic Engineering, Changchun University of Technology, Changchun, Jilin, 130012, China

^c Beijing Institute of Nanoenergy and Nanosystems, Chinese Academy of Sciences, Beijing, 100083, China

^d School of Materials Science and Engineering, Georgia Institute of Technology, Atlanta, GA 30332-0245, United States

ARTICLE INFO

Article history:

Received 11 August 2019

Received in revised form 18 October 2019

Accepted 18 October 2019

Available online xxxx

Keywords:

Rotational speed sensor

Integration

Bearing

Triboelectric nanogenerator

Industrial application

ABSTRACT

A rotational speed sensor is of great importance for the development of modern industrial automation. The reliability, integration, measuring range and accuracy are key characteristics to its application. We report a triboelectric rotational speed sensor that is integrated into a bearing (TRSS) and is composed mainly of a bearing seat, a bearing, an adjusting ring, a rotor and a stator. The sensor-output stability can be improved significantly by modifying the bearing's structural characteristics. Periodic electric signals are generated by rotating friction between the copper grating on the rotor and a polytetrafluoroethylene film on the stator surface to induce electron transfer on the copper electrode. A comparison of the analysis of the output signal with a commercial sensor proved that TRSS can be used to measure the rotational speed from 10–1000 rpm with an error below 0.3% and an excellent linearity. Therefore, TRSS is reliable and consistent by verifying the measurement accuracy of the sensors with different sizes. We applied this sensor in an industrial application and demonstrated the application prospects of TRSS.

© 2019 Elsevier Ltd. All rights reserved.

1. Introduction

In modern industrial automation production, rotational speed sensors are required for rotational accuracy, such as in computer-numerical-controlled (CNC) machine tools, printing equipment and robot rotational joints. The main encoders that are used for rotational speed measurement are based on an optoelectrical transformation or electromagnetic induction. [1–3] The structures of these commercial sensors have been solidified and must be equipped with the corresponding coupling and fixed support for installation, which requires additional installation space without the option for integration into mechanical parts. These properties are not conducive to equipment miniaturization and integration.

The triboelectric nanogenerator (TENG) was invented by Wang and co-workers in 2012, [4] and can generate an electrical output based on triboelectrification and electrostatic induction in response to an external mechanical stimulation. [5] In the application of Maxwell displacement current theory in the field of

energy and sensors, [6–11] TENG has been used to harvest wind energy, [12,13] ocean energy and mechanical energy because of its low cost, simple structure, pollution-free nature and high energy conversion efficiency. [14–18] An analysis of the TENG output signal allows for the dynamic and static mechanical stimulation to be detected. Based on these principles, [19–23] sensors have been designed, including vibration sensors, [24,25] tactile mapping, [26,27] acceleration sensing and angle detection. [28–31] Only a few papers have explored the use of TENG to detect the rotational speed. Jing et al. proposed a sensor that can measure linear and rotational motion, [32] which provides a good reference and guidance for us to develop the triboelectric rotational speed sensor.

A simplification of the structure of the rotational speed sensor makes it easy to integrate. We propose a triboelectric rotational speed sensor that is integrated into a bearing (TRSS) and that can measure the rotational speed by making minor changes to the structure of the original bearing seat. Equipment space savings are provided compared with the original structure. The bearing is a type of rotating component that is used extensively in mechanical equipment. The high rotation accuracy and shielding external load interference characteristics of the bearing, the rotation accuracy and the sensor can be guaranteed, and the rotational speed can be calculated by processing and converting the sensor output

* Corresponding authors.

** Corresponding author at: School of Materials Science and Engineering, Georgia Institute of Technology, Atlanta, GA 30332-0245, United States.

E-mail addresses: xiezhijie@hit.edu.cn (Z. Xie), cth@ccut.edu.cn (T. Cheng), zlwang@gatech.edu (Z.L. Wang).

<https://doi.org/10.1016/j.eml.2019.100595>

2352-4316/© 2019 Elsevier Ltd. All rights reserved.

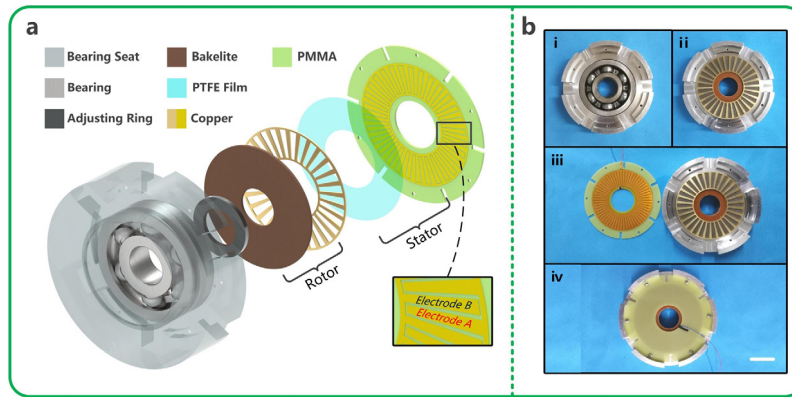


Fig. 1. Structure design of the TRSS. (a) Schematic illustrations of the functional components of TRSS, which consists of a bearing seat, a bearing, an adjusting ring, a rotor and a stator. (b) TRSS assembly sequence (scale bar, 3 cm).

signal. After systematic research, the manufactured sensor can be measured at 10–1000 rpm with an error of less than 0.3%, which has great linearity and can adapt to different bearing sizes. This work presents progress in the application of triboelectric sensors.

2. Results and discussion

2.1. Structure and working principle of TRSS

The basic configuration of the TRSS is illustrated schematically in Fig. 1a. The TRSS frictional electrification is composed mainly of two coaxially mounted components, namely, a rotor and a stator. The rotor is a double-layer structure that consists of a bakelite base and a copper grating. The copper grating is a group of radially arranged sectors that are separated by equal intervals. Each sector unit has a central angle of 6° , and the copper grating has a total of 30 units (the basis for the parameter design can be found at the end of this section). The stator consists of a layer of polytetrafluoroethylene (PTFE) film as an electrification material, a layer of copper electrodes and a circular polymethyl methacrylate (PMMA) substrate. The electrode layer is separated by fine grooves to form two parts: electrodes A and B. Each part of the electrode layer is a fixed-sector area of the radial array and is connected on the circumference to form two interlocking sector copper electrode combs. The pattern on each part is consistent with that on the rotor. Fig. 1a shows an enlarged view of the electrodes with several radially aligned sector-shaped electrodes that are distributed uniformly along the circumference. The rotor and stator are integrated into the bearing through the bearing seat. The assembly sequence of the TRSS is shown in Fig. 1b, where the inner ring of the bearing seat matches the outer ring of the bearing. A stepped surface is provided with six threaded holes to facilitate the fixing of the stator by bolts. The adjusting ring is used mainly to adjust the distance between the rotor and the stator to ensure complete contact. A detailed description of the TRSS is presented in the Experimental Section.

The TRSS generates electricity by rotating friction between the rotor and the stator. During this period, the electrostatic coupling effect of the friction electrification induces the alternating flow of charges between the two electrode networks. The generation process is described in detail by the basic unit in Fig. 2. The working mechanisms are explained by schematic illustrations of the potential distribution in the open-circuit condition simulated by COMSOL Multiphysics software. For convenience of explanation, three representative contact states are defined, i.e., the initial state of alignment between the rotor sector and electrode A (Fig. 2a), the transition state of rotation from the initial position

to the final position (Fig. 2b) and the final state of alignment between the rotor sector and electrode B (Fig. 2c).

When the rotor rotates around the axis, the copper grating slides along the PTFE film surface and generates and accumulates friction charges on the surfaces of two friction materials. Because the material electronegativity is different, PTFE accumulates negative friction charges on the surface. According to the law of conservation of charge, the surface of the copper grating will have a positive friction charge, and the surface area of the copper grating is only half that of PTFE, so the positive charge density on the surface of the rotor is twice that of the negative charge on the stator. Under open-circuit conditions, electrons cannot be transferred between electrodes. Therefore, the open-circuit voltage (V_{OC}) is the potential difference between the two electrodes. In the initial state of rotation, electrodes A and B reach the maximum and minimum potential, respectively, which corresponds to the maximum open-circuit voltage. When the rotor rotates further, the voltage decreases accordingly. When it reaches the midpoint, the open-circuit voltage decreases to zero, and further rotation generates the reverse voltage. When the two electrodes are connected by wires, electrons can flow back and forth between the electrodes because of the electrostatic induction. Therefore, the alternating-current output will be generated during the continuous relative rotation of the rotor.

Based on Wang's work, [21] the peak open-circuit voltage is determined by d and σ_0 :

$$V_{OC} = \frac{4d \cdot \sigma_0}{\epsilon_0 \epsilon_r} \quad (1)$$

where d is the PTFE film thickness, σ_0 is the triboelectric charge density on the PTFE film surface, ϵ_0 is the vacuum dielectric constant and ϵ_r is the relative dielectric constant of PTFE.

The characteristic (output) frequency (f) of the equipment depends on the number of gratings (N) and the rotational speed (n) of the rotor:

$$f = N \cdot \frac{n}{60} = \frac{180}{\Delta\theta} \cdot \frac{n}{60} = \frac{3n}{\Delta\theta} \quad (2)$$

where $\Delta\theta$ is the center angle ($^\circ$) of the copper grating. The number of gratings for photoelectric coding that are used to measure the rotational speed tends to lie between 10 and 60. Therefore, in this work, we chose N and $\Delta\theta$ to be 30 and 6° , respectively.

2.2. Processing of the output signal

In industry, rotational speed sensors tend to be used to measure speeds above 10 rpm for constant speed control, and angle

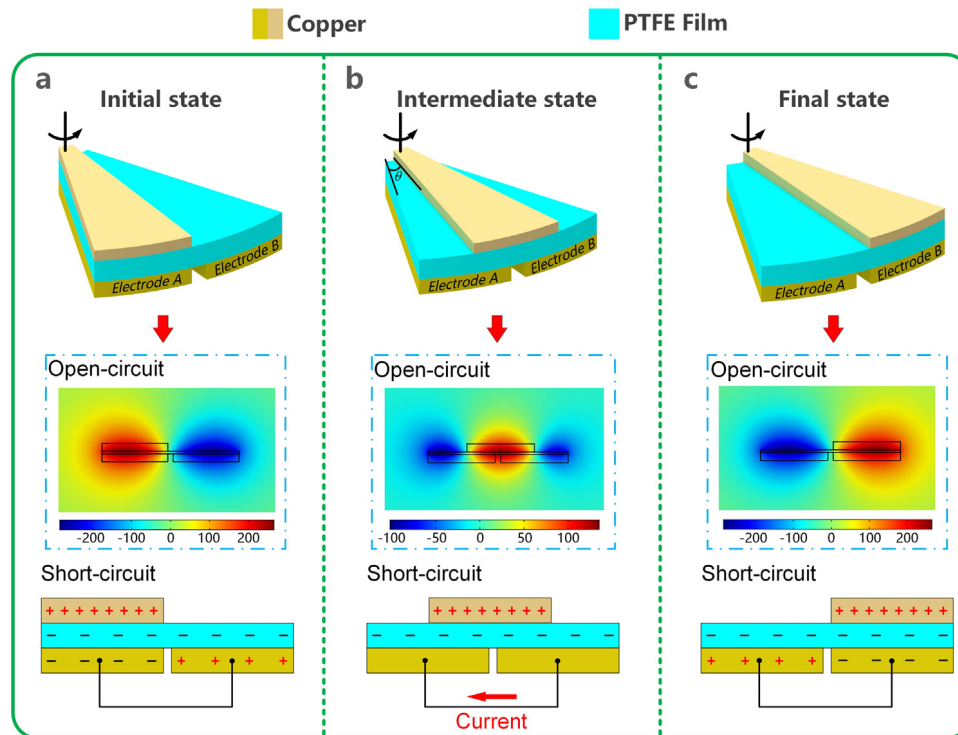


Fig. 2. Schematic diagrams of the working principle of the TRSS. The diagrams provide a schematic of the TRSS's working state in a half cycle, current and charge distribution in a short-circuit condition (lower), and the potential distribution that is simulated by COMSOL in an open-circuit condition (upper) in (a) the initial state, (b) the intermediate state and (c) the final state.

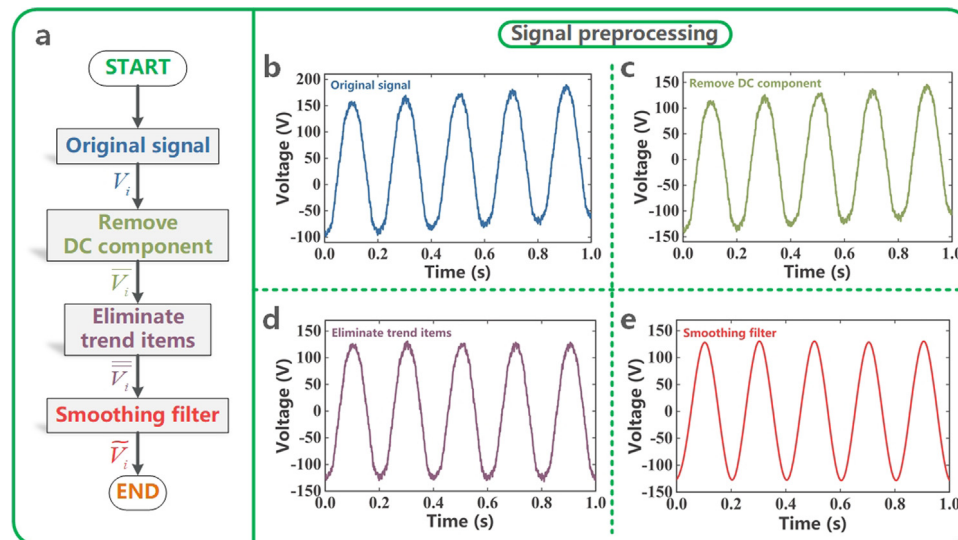


Fig. 3. Preprocessing of the original signal. (a) Flow chart of signal preprocessing. (b) Original signal of open-circuit voltage measured at 10 rpm. (c) Signal after DC component removal. (d) Signal after trend item removal. (e) Signal after smoothing.

sensors tend to be used for positioning control when the speed is below 10 rpm. Therefore, for TRSS, we chose 10 rpm as the starting speed for the electrical signal measurement. According to the size of the 6406 standard bearing, the inner and outer rotor diameters were selected as 47 mm and 100 mm, respectively (more information can be found in the Experimental Section). Fig. 3b shows the original signal of the open-circuit voltage at a rotational speed of 10 rpm. The measured signal has the following main problems. First, the signal deviates from the origin (the mean measured signal is not zero), that is, there is a direct-current (DC) component, which is caused by the measurement characteristics of the instrument itself. Second, the signal slopes

and has a trend term, possibly because of the servo interference during the testing process. Third, local distortions, such as sawtooths, spikes and burrs occur because of the mixing of noise signals. To obtain regular signals, eliminate noise interference and ensure the accuracy of subsequent analysis, it is necessary to preprocess the original signal.

Fig. 3a shows the flow chart of the signal preprocessing. We must remove the DC component of the original signal and perform zero-average preprocessing on the signal. The concrete method is to average the resultant sampling discrete sequence

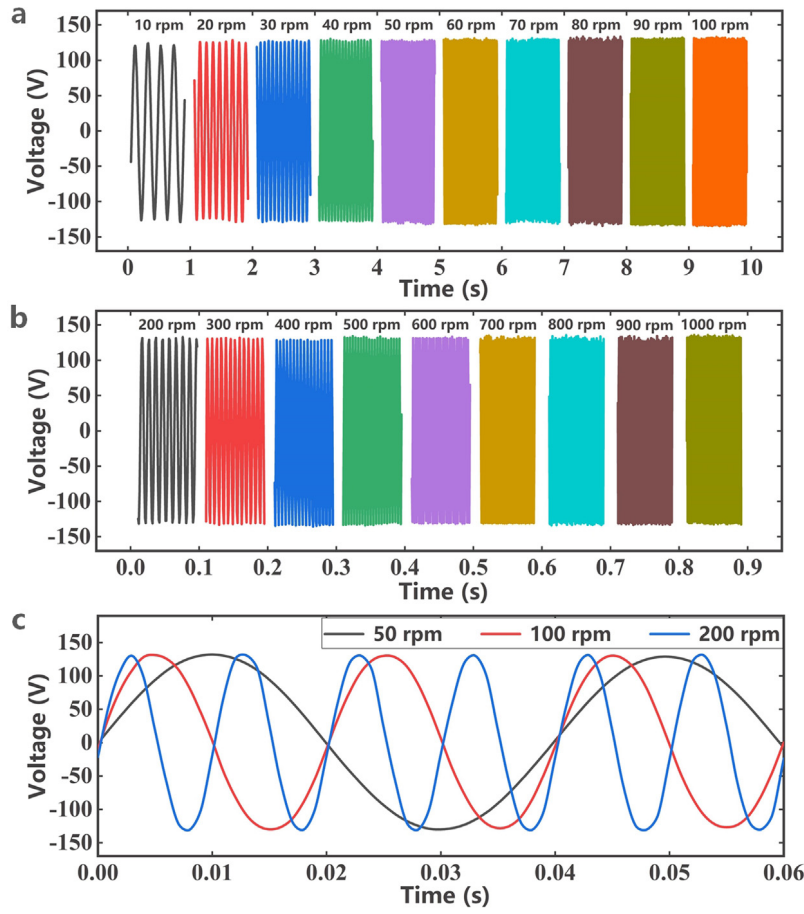


Fig. 4. Open-circuit voltage of TRSS. (a) and (b) open-circuit voltage (V_{oc}) at different rotational speeds. (c) Varying rotational speeds generate varying signal cycle lengths.

$V_i, i = 1, 2, \dots, M$:

$$\hat{V}_i = \frac{1}{M} \sum_{i=1}^M V_i \quad (3)$$

and define a new signal $\{\bar{V}_i\}, i = 1, 2, \dots, M$:

$$\bar{V}_i = V_i - \hat{V}_i \quad (4)$$

In this case, $\{\bar{V}_i\}$ is a zero-mean signal, and the signal waveform is shown in Fig. 3c.

The trend term still exists in the signal after the DC component removal. The most commonly used method for eliminating trend terms is the least-squares method, which can minimize the sum of squares of residual errors. The trend term is a slowly changing signal, which can be fitted by a polynomial. Once the polynomial is determined, an approximate real signal can be obtained by subtracting the polynomial from $\{\bar{V}_i\}$. We construct a polynomial of order P :

$$T_i = a_0 + a_1 i + a_2 i^2 + \dots + a_P i^P = \sum_{k=0}^P a_k i^k \quad (5)$$

By using this polynomial to fit $\bar{V}_i, i = 1, 2, \dots, M$, there must be a fitting error, and the sum of the squares of the total errors is:

$$E = \sum_{i=1}^M [T_i - \bar{V}_i]^2 = \sum_{i=1}^M [\sum_{k=0}^P a_k i^k - \bar{V}_i]^2 \quad (6)$$

To minimize E , the derivatives of E for each order can be zero, that is:

$$\frac{\partial E}{\partial a_r} = 0 \quad r = 0, 1, 2, \dots, P \quad (7)$$

Insert $\bar{V}_i, i = 1, 2, \dots, M$ into Eq. (7) to determine the polynomial coefficient a_0, a_1, \dots, a_P , so that the polynomial T_i can be determined. By subtracting T_i , a new signal $\{\tilde{V}_i\}, i = 1, 2, \dots, M$ can be obtained as follows:

$$\tilde{V}_i = \bar{V}_i - T_i \quad (8)$$

The signal waveform after eliminating the trend term is shown in Fig. 3d.

Finally, it is necessary to eliminate the interference of the noise signal and to improve the smoothness of the curve. The signal was smoothed by the linear moving average method. The method modifies the amplitude of the point according to the amplitude of the nearby sampling point, to de-noise the waveform. The basic formula of the average method is:

$$\tilde{V}_i = \sum_{k=-S}^S h_k \bar{V}_{i-k} \quad (i = 1, 2, \dots, M) \quad (9)$$

where \bar{V} is the previously obtained data, \tilde{V}_i is the smoothed data, M is the number of data points, S is the average number of points and h_k is the weighted average factor.

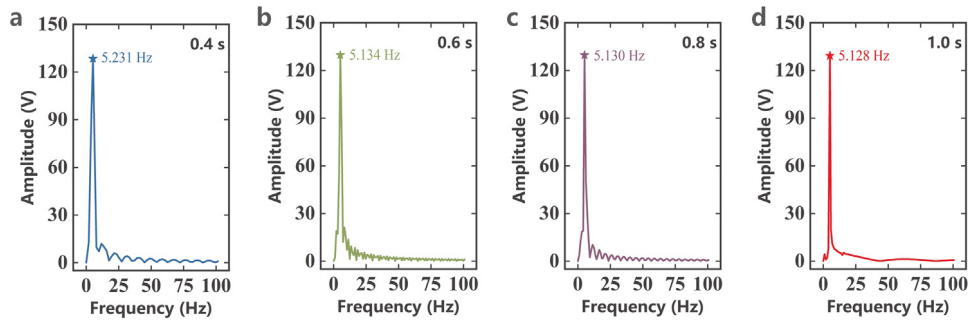


Fig. 5. Spectrum charts of different sampling times at 10.240 rpm. (a)–(d) Sampling times of 0.4 s, 0.6 s, 0.8 s and 1 s, with errors of 2.2%, 0.27%, 0.20% and 0.16%, respectively.

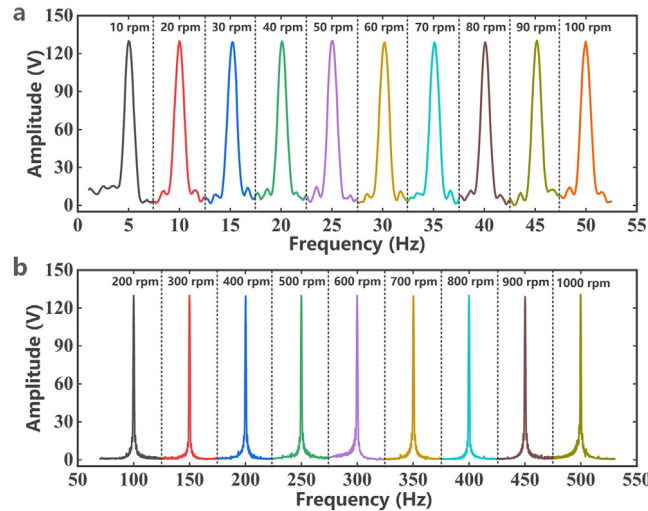


Fig. 6. Characteristic frequency analysis of TRSS. (a)–(b) Spectrum charts at different rotational speeds.

The weighted average factor must satisfy the following formula:

$$\sum_{k=-S}^S h_k = 1 \quad (10)$$

Where $h_k = 1/(2S + 1)(n = 0, 1, 2, \dots, S)$, that is

$$\tilde{V}_i = \frac{1}{2S + 1} \sum_{k=-S}^S \overline{V_{i-k}} \quad (11)$$

Here we take the five-point weighted averaging method ($S = 2$) to smooth the signal. The endpoint is obtained by interpolation, and the final signal is shown in Fig. 3e. Later, $\{\tilde{V}_i\}$ will be used as the starting point for subsequent analysis.

Fig. 4a and b present the open-circuit voltage of the TRSS at different rotational speeds (10–1000 rpm) after signal pre-treatment. With the increase in rotational speed, the open-circuit voltage is almost constant at an amplitude of 130 V, because the open-circuit voltage is related only to material and equipment structure and is independent of the rotational speed according to Eq. (1).

To analyze the characteristics of the output signal, the open-circuit voltage output at three typical rotational speeds is plotted in Fig. 4c. The signal itself has an obvious regularity, and the period of the generated electrical signals is consistent with that of the driving motor. According to Eq. (2), the corresponding rotational speed can be calculated if the characteristic (output) frequency of the output signal is given. This reflects the possibility of using the TRSS as a rotational speed sensor.

To obtain the actual characteristic frequency, it is necessary to perform Fast Fourier Transform (FFT) on the output signal. Through FFT, the time domain signal can be converted rapidly to a frequency domain signal and the characteristic frequency of the signal can be extracted. The accuracy of the characteristic frequency depends on the number of complete cycles in the sampling time. In theory, a more accurate extracted characteristic frequency is obtained with the inclusion of more periodic signals. Fig. 4 shows that with an increase in rotational speed, more complete cycles are included in the same sampling time. Therefore, the set sampling time should be guaranteed to have a sufficient measurement accuracy at the lowest rotational speed. Fig. 5 shows the spectrum analysis results at different sampling times when the rotational speed is 10.240 rpm (measurement by commercial sensor), and the corresponding characteristic frequency can be calculated to be 5.120 Hz according to Eq. (2). The results reflect that with the increase in sampling time, the characteristic frequency is closer to the true value. However, too long a sampling time is not conducive to real-time calculation and reduces the processing efficiency. Calculations show that the error rate decreases from 2.2% to 0.27% when the sampling time increases from 0.4 s to 0.6 s, and when the sampling time increases, the accuracy does not improve significantly. Therefore, to balance the accuracy and efficiency, 0.6 s was chosen as the uniform sampling time.

By setting the sampling time to 0.6 s, an FFT transformation could be performed on the preprocessed signal, and the spectrum charts at different rotational speeds were obtained as shown in Fig. 6. The amplitude characteristics of the corresponding characteristic frequencies are obvious, with almost no noise

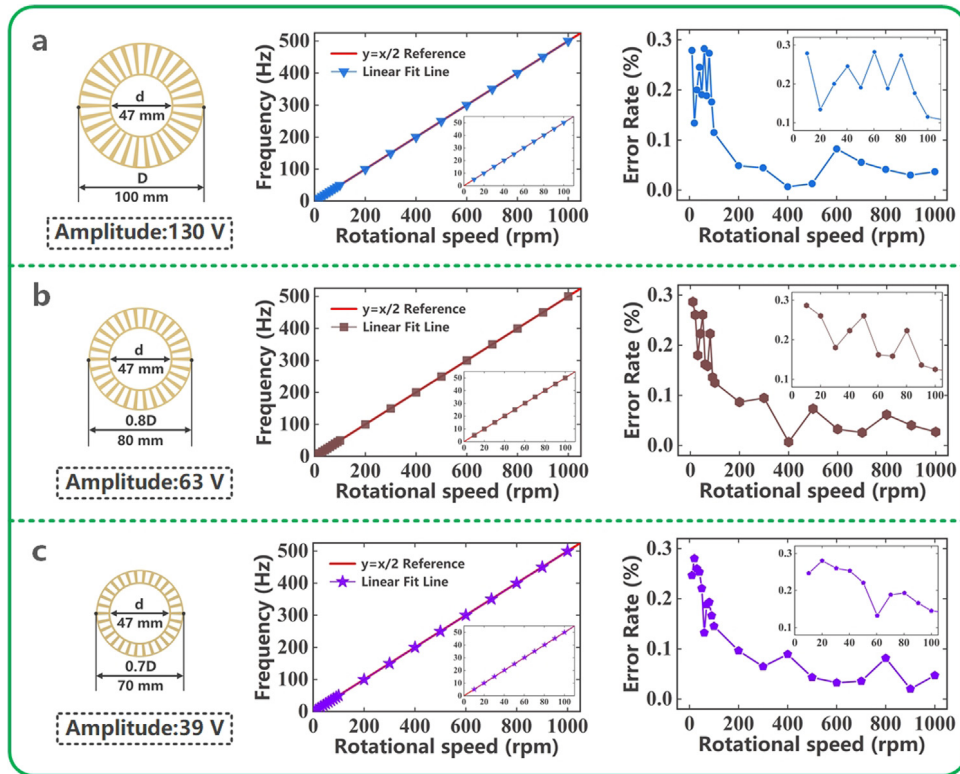


Fig. 7. Consistency verification of measurement results for different structural parameters. (a)–(c) Linearity and error rate for different structural parameters.

interference, which confirms that TRSS has a distinct and stable periodic output.

To understand the sensing characteristics of TRSS, the characteristic frequencies at different rotational speeds were extracted to fit the straight line and compared with the theoretical straight line, as shown in Fig. 7a. The fitting straight line is almost identical to the theoretical reference line, and shows a great linearity. By comparing the rotational speed that was calculated from the characteristic frequency with the values that were measured by a commercial sensor, the error rate curve at different rotational speeds was obtained. The curve shows that, although the error rate fluctuates with the change in speed because of the installation error, a high measurement accuracy can be guaranteed. For a measured speed at 10–100 rpm, the error rate can be controlled at 0.1% to 0.3%. Above 100 rpm, the error rate can be controlled at 0.1% or less. Similar results can be obtained based on an analysis of the short-circuit current output (detailed discussion can be found in the Supporting Information). We also validated the consistency of the sensor measurements for different sizes. By keeping the inner diameter of the rotor unchanged at 47 mm, the outer diameter was reduced to 80 mm and 70 mm, respectively, and the corresponding open-circuit voltage amplitudes are 63 V and 39 V, respectively. The fitted lines and error rate curves are plotted in Fig. 7b and c. When the number of gratings is constant, the measurement accuracy of the sensor is almost unaffected by the size, which illustrates the excellent consistency and reliability. Therefore, the measurement accuracy does not change and can adapt to different bearing sizes.

3. Industrial application

TRSS has been proven to have a stable and accurate periodic output, and it is an ideal choice as a rotational speed sensor. Therefore, we used TRSS for industrial application to measure the rotational speed of a real mechanical shafting component

and compared it with a commercial sensor. Fig. 8a and b show the most commonly used industrial shafting arrangement, which includes a stepped shaft, support pedestals, a TRSS, torque and speed sensors, a coupling and a servo motor with an overall size of 920 mm \times 166 mm \times 182 mm. The output shaft of the servo motor was connected to the input shaft of the torque and speed sensors through coupling, and the output shaft of the sensor was also connected with the stepped shaft through coupling. The support pedestals at both ends of the stepped shaft were used to reduce the runout of the shaft and to ensure rotational stability. All mechanical parts were fixed on the aluminum profile by bolts. We developed rotational speed accuracy test software as shown in Fig. 8c, which can collect and process the output signals and calculate the rotational speed. By comparing the measured commercial sensor values (torque and speed sensors), the error rate at different rotational speeds can be displayed in real time. The live demonstration in video S1 (Support Information) confirms that TRSS can be used to measure the rotational speed of shafting with a high accuracy. More importantly, the TRSS validated the feasibility of integrating the TENG into mechanical parts for sensing measurement and has bright prospects for application.

4. Conclusions

We have demonstrated a TRSS that was integrated into a bearing. Compared with commercial sensors, the TRSS has a simple structure, requires only a small installation space and can be integrated easily into mechanical parts to improve the equipment integration. The sensing characteristics of the TRSS were studied through signal processing. The experimental results show that the characteristic (output) frequency exhibits a linear relationship with the rotational speed, with almost no linear error. By using the corresponding relationship between the frequency and the rotational speed, the TRSS can be used to measure the rotational speed of 10–1000 rpm. When the rotational speed is below 100

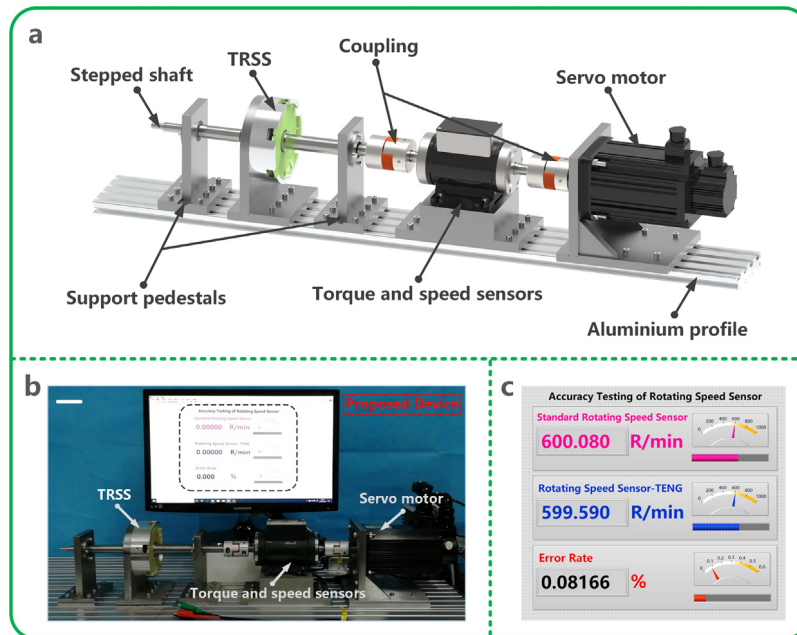


Fig. 8. Industrial application of TRSS in rotational speed measurement. (a) Most commonly used shafting arrangement in the industry (b) Photograph of shafting system (scale bar, 5 cm). (c) Interface of rotational speed accuracy test software.

rpm, the error rate can be controlled below 0.3%. Above 100 rpm, the error rate can be controlled at 0.1% or less, which meets the precision requirements of most industrial applications. By verifying the measurement accuracy of sensors with different sizes, it has been proven that TRSS has a size adaptability, reliability and consistency. We applied this sensor in an industrial application, compared the results with the measured values of a commercial sensor in real time and confirmed that TRSS can be used to measure the rotational speed of shafting with a high accuracy and has bright prospects for application.

5. Experimental sections

5.1. Fabrication of the TRSS

As shown in Fig. 1, the TRSS was composed of a bearing seat, a bearing, an adjusting ring, a rotor and a stator. The selected bearing model was a 6406 standard component. Its inner diameter, outer diameter and width were 30 mm, 90 mm and 23 mm, respectively. The bearing seat and adjusting ring were machined to ensure accuracy and a match with the bearing, in which the inner ring of the bearing seat and the outer ring of the bearing were matched, and the two ends of the adjusting ring were contacted closely with the end face of the bearing inner ring and the end face of the rotor, respectively.

The TRSS rotor consisted of a bakelite base and a copper grating. The detailed fabrication process was as follows: (1) a bakelite ring was cut by a laser cutting machine as the matrix. Its inner diameter, outer diameter and thickness were 30 mm, 100 mm and 2 mm, respectively. (2) By cutting copper grating with a laser cutting machine, an inner diameter, outer diameter and thickness of 47 mm, 100 mm and 1 mm, respectively, were achieved. The circumferential distribution was of 30 radially aligned sector areas, the radial length was 23 mm, and the central angle was 6° . The outer diameters were set to 70 mm and 80 mm, respectively, and the other sizes remained unchanged. The two copper gratings were cut in the same way. (3) The copper grating was bound to the matrix with 3M double-sided adhesive, and kept for 24 h until fully bonded.

The stator had two identical electrode units, which were arranged in opposite directions to form two interlocking fan-shaped electrode combs. The fan-shaped pattern of each unit was the same as that of the rotor. The electrode was made from 35 μm -thick copper, which was fabricated by industrial printed circuit board (PCB) technology and packaged on a 1.6 mm-thick circuit board substrate. An 80 μm -thick PTFE film was adhered to the electrode surface.

5.2. Measurement

Speed and Torque Sensors (JN338-AE, Sanjing, China) are connected with AC Servo Motor (110JASM5102K, Yixing, China) through coupling. It is used to measure input rotational speed in real time and convert the measured frequency signal into standard voltage signal through transmitter (JN338-F/V, Sanjing, China). Electrical measurements of rotational speed sensor were carried out by electrometer (6514, Keithley, USA). The signal lines of the transmitter and electrometer are connected to the data acquisition system (PCI-6259, National Instruments, USA) and finally input to the computer. The software platform was constructed based on LabVIEW, which was capable of realizing real-time data acquisition control and analysis.

Declaration of competing interest

The authors declare that they have no known competing financial interests or personal relationships that could have appeared to influence the work reported in this paper.

Acknowledgments

Zhijie Xie, Jiewei Dong and Yikang Li contributed equally to this work. The authors are grateful for financial support from the National Key Research and Development Program of China (MB20170134), and the National Natural Science Foundation of China (grant numbers 51805109 and U1737204).

Appendix A. Supplementary data

Supplementary material related to this article can be found online at <https://doi.org/10.1016/j.eml.2019.100595>.

References

- [1] L. Luan, R.D. Evans, N.M. Jokerst, R.B. Fair, *IEEE Sens. J.* 8 (2008) 628.
- [2] C. Ciminelli, F. Dell'Olio, C.E. Campanella, M.N. Armenise, *Adv. Opt. Photonics* 2 (2010) 370.
- [3] Z. Zhang, F. Ni, Y. Dong, M. Jin, H. Liu, *Sensors Actuators A* 194 (2013) 196.
- [4] F.-R. Fan, Z.-Q. Tian, Z.L. Wang, *Nano Energy* 1 (2012) 328.
- [5] C. Zhang, W. Tang, C. Han, F. Fan, Z.L. Wang, *Adv. Mater.* 26 (2014) 3580.
- [6] Z.L. Wang, *Mater. Today* 20 (2017) 74.
- [7] S.L. Zhang, M. Xu, C. Zhang, Y.-C. Wang, H. Zou, X. He, Z. Wang, Z.L. Wang, *Nano Energy* 48 (2018) 421.
- [8] R. Liu, X. Kuang, J. Deng, Y.C. Wang, A.C. Wang, W. Ding, Y.C. Lai, J. Chen, P. Wang, Z. Lin, *Adv. Mater.* 30 (2018) 1705195.
- [9] C. He, W. Zhu, G.Q. Gu, T. Jiang, L. Xu, B.D. Chen, C.B. Han, D. Li, Z.L. Wang, *Nano Res.* 11 (2018) 1157.
- [10] Y. Chen, Y.C. Wang, Y. Zhang, H. Zou, Z. Lin, G. Zhang, C. Zou, Z.L. Wang, *Adv. Energy Mater.* 8 (2018) 1802159.
- [11] H. Ryu, J.H. Lee, U. Khan, S.S. Kwak, R. Hinchet, S.-W. Kim, *Energy Environ. Sci.* 11 (2018) 2057.
- [12] T. Cheng, Y. Li, Y.-C. Wang, Q. Gao, T. Ma, Z.L. Wang, *Nano Energy* 60 (2019) 137.
- [13] H. Lin, M. He, Q. Jing, W. Yang, S. Wang, Y. Liu, Y. Zhang, J. Li, N. Li, Y. Ma, *Nano Energy* 56 (2019) 269.
- [14] Z.L. Wang, T. Jiang, L. Xu, *Nano Energy* 39 (2017) 9.
- [15] G.Q. Gu, C.B. Han, J.J. Tian, C.X. Lu, C. He, T. Jiang, Z. Li, Z.L. Wang, *ACS Appl. Mater. Interfaces* 9 (2017) 11882.
- [16] G.X. Liu, W.J. Li, W.B. Liu, T.Z. Bu, T. Guo, D.D. Jiang, J.Q. Zhao, F.B. Xi, W.G. Hu, C. Zhang, *Adv. Sustain. Syst.* 2 (2018) 1800081.
- [17] C. Wu, R. Liu, J. Wang, Y. Zi, L. Lin, Z.L. Wang, *Nano Energy* 32 (2017) 287.
- [18] M. Xu, P. Wang, Y.C. Wang, S.L. Zhang, A.C. Wang, C. Zhang, Z. Wang, X. Pan, Z.L. Wang, *Adv. Energy Mater.* 8 (2018) 1702432.
- [19] S. Niu, S. Wang, L. Lin, Y. Liu, Y.S. Zhou, Y. Hu, Z.L. Wang, *Energy Environ. Sci.* 6 (2013) 3576.
- [20] S. Niu, Y. Liu, S. Wang, L. Lin, Y.S. Zhou, Y. Hu, Z.L. Wang, *Adv. Mater.* 25 (2013) 6184.
- [21] G. Zhu, J. Chen, T. Zhang, Q. Jing, Z.L. Wang, *Nature Commun.* 5 (2014) 3426.
- [22] L. Lin, S. Wang, S. Niu, C. Liu, Y. Xie, Z.L. Wang, *ACS Appl. Mater. Interfaces* 6 (2014) 3031.
- [23] S. Niu, Y. Liu, S. Wang, L. Lin, Y.S. Zhou, Y. Hu, Z.L. Wang, *Adv. Funct. Mater.* 24 (2014) 3332.
- [24] J. Chen, G. Zhu, W. Yang, Q. Jing, P. Bai, Y. Yang, T.C. Hou, Z.L. Wang, *Adv. Mater.* 25 (2013) 6094.
- [25] X. Chen, H. Guo, H. Wu, H. Chen, Y. Song, Z. Su, H. Zhang, *Nano Energy* 49 (2018) 51.
- [26] X. Wang, H. Zhang, L. Dong, X. Han, W. Du, J. Zhai, C. Pan, Z.L. Wang, *Adv. Mater.* 28 (2016) 2896.
- [27] X. Pu, M. Liu, X. Chen, J. Sun, C. Du, Y. Zhang, J. Zhai, W. Hu, Z.L. Wang, *Sci. Adv.* 3 (2017) e1700015.
- [28] B. Zhang, L. Zhang, W. Deng, L. Jin, F. Chun, H. Pan, B. Gu, H. Zhang, Z. Lv, W. Yang, *ACS Nano* 11 (2017) 7440.
- [29] Q.F. Shi, H. Wu, H. Wang, H.X. Wu, C.K. Lee, *Adv. Energy Mater.* 7 (2017).
- [30] M. Han, X.-S. Zhang, X. Sun, B. Meng, W. Liu, H. Zhang, *Sci. Rep.* 4 (2014) 4811.
- [31] Y. Wu, Q. Jing, J. Chen, P. Bai, J. Bai, G. Zhu, Y. Su, Z.L. Wang, *Adv. Funct. Mater.* 25 (2015) 2166.
- [32] Q. Jing, G. Zhu, W. Wu, P. Bai, Y. Xie, R.P. Han, Z.L. Wang, *Nano Energy* 10 (2014) 305.